Supplementary Information

1 Supplementary Discussion

1.1 S1: ToF Data Treatment

Ion time-of-flight (iToF) mass spectrometric data were analysed using a custom Python workflow. Raw data were loaded on a per-run basis, selecting digitizer traces from the SQS UTC digitizer, signals from both the SQS and tunnel XGM, and the undulator photon energy readback. Only trains for which all required data sources were present were retained; the corresponding train IDs were determined once per run and cached for reproducibility.

Digitizer traces were extracted for the iToF channel and reshaped into individual pulses according to the known bunch structure. For each pulse, a baseline correction was applied by subtracting, for each periodic sampling position, the mean of the corresponding samples within a predefined baseline window. Event detection in the corrected traces was performed using a constant-fraction discriminator (CFD) algorithm with fixed threshold and delay parameters. The resulting CFD edge times were digitized to integer iToF bins and accumulated into per-pulse histograms.

Photon-energy–resolved spectra were constructed by binning pulses according to the photon energy derived from the undulator readback. A hard energy window was applied to select pulses within a fixed interval above each target photon energy. Within each photon-energy bin, additional intensity filtering was performed using the SQS and tunnel XGM signals: only pulses with intensities lying within one standard deviation of the mean of the preselected distribution were retained, suppressing fluctuations in FEL pulse energy. The digitized iToF spectra were then summed over all accepted pulses and normalized by the number of contributing pulses, yielding an average count spectrum per photon energy. Statistical uncertainties were estimated assuming Poisson counting statistics and propagated accordingly.

Time-of-flight axes were converted to mass-over-charge (m/q) coordinates using a quadratic calibration, $m/q = k(t - t_0)^2$, where the calibration parameters were obtained by fitting known reference peak positions. For visualization of two-dimensional photon-energy–dependent charge-density maps, the normalized iToF spectra were multiplied by the corresponding iToF values and arranged into a matrix as a function of photon energy and iToF. All analysis steps, including train selection, filtering criteria, normalization procedures and calibration, were applied identically to all runs to ensure internal consistency across the dataset.

1.2 S2: Volume Integration of XATOM Simulations

To enable a meaningful comparison between ab initio XATOM simulations and experimentally measured ion yields, the theoretical results were volume-integrated to account for the spatial intensity distribution of the focused XFEL beam. While XATOM provides ion yields for a single, well-defined photon number (i.e., peak intensity), the experiment probes an extended interaction volume in which atoms experience a continuum of local intensities due to the transverse profile of the FEL focus. We assume this transverse profile to be Gaussian. Consequently, the experimentally observed charge-state distributions represent an incoherent sum over contributions from different intensities, weighted by the corresponding interaction volume. Volume integration is therefore essential to place theory and experiment on the same physical footing.

XATOM output files were parsed directly from text-based simulation results. For each simulation file, the photon energy and photon number were extracted from the filename, and the charge-state–resolved ion yields were read using regular-expression matching. For each photon energy and photon number, the ion yields were normalized such that the sum over all included charge states was unity, ensuring that subsequent volume integration preserved relative charge-state probabilities rather than absolute yields.

Volume integration was implemented following a standard Gaussian-beam formalism. All photon numbers present in the dataset were collected and sorted in descending order. Using the maximum photon number as a reference, analytical volume-weighting factors were computed for each intensity interval based on differences of the error function, $erf(-ln(\frac{I}{Imax}))$. These F-factors represent the fractional interaction volume associated with atoms experiencing intensities between successive photon-number thresholds. The final interval, extending from the lowest simulated intensity down to zero, was treated analytically to ensure that the total volume weight summed to unity.

For each photon energy, volume-integrated charge-state distributions were constructed by accumulating the normalized ion yields from a given photon number and all lower photon numbers, each weighted by its corresponding factor. The resulting summed distributions were renormalized to unity to yield volume-integrated ion yields that can be compared to experimental charge-state fractions. This procedure was repeated independently for all photon energies and reference photon numbers present in the dataset.

The volume-integrated results were subsequently reorganized into array form for visualization and analysis. All steps in the volume-integration workflow were applied uniformly across the dataset to ensure internal consistency.

1.3 S3: Photoionisation Cross-Cection Calculations

The atomic photoionisation cross sections depicted for the various Fe charge states in Figure 2 were calculated using the Cowan code within the Hartree-Fock approximation with relativistic extensions, following the method described in [1, 2]. For all ionic states, the initial and excited states are described by the configurations listed in Table 1 on page 3 taking into account configuration interactions between them. The cross section was always calculated for the ground state of the corresponding ion. Spectra of possible excited states have a similar shape as shown in [3, 4].

initial	excited
$2p^6 3s^2 3p^6 3d^n 4s^2$	$2p^5 3s^2 3p^6 3d^{n+1} 4s^2$
$2p^6 3s^2 3p^6 3d^{n+1} 4s^1$	$2p^5 3s^2 3p^6 3d^{n+2} 4s$
$2p^6 3s^2 3p^6 3d^{n+2}$	$2p^5 3s^2 3p^6 3d^{n+3}$

Table 1: Configurations.

The Auger-Meitner decay was calculated for the channels listed in the Table 2 on page 3.

$3s^{-2}$
$3s^{-1}3p^{-1}$
$3p^{-2}$
$3d^{-2}$
$3s^{-1}3d^{-1}$
$3p^{-1}3d^{-1}$

Table 2: Configurations Auger-Meitner decay channels.

For higher charged states, not all decay channels are possible if the number of $3d$ electrons becomes too small. Possible decay channels including the $4s$ electrons were not taken into account due to the much smaller Coulomb matrix elements. From the Auger-Meitner rates, the line width of all resonances were then calculated.

2 Supplementary Figure

2.1 S1: Additional Ion Fragment Spectra

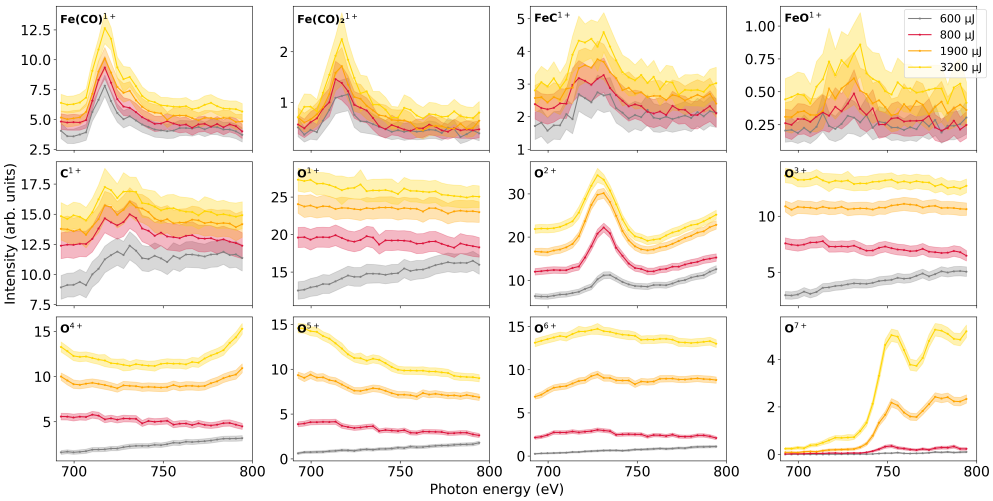

Fig. 1: Collection of selected fragment cation signals from the $Fe(CO)_5$ sample recorded over the photon-energy range from 695 eV to 800 eV for pulse energies of 600 µ J, 800 µ J, 1900 µ J, and 3200 µ J. Note that some signals, such as O^{2+}, are affected by an iron cation background, offset in amplitude and showing the corresponding iron resonance. For iron carbonyl fragments, the resonance profiles and positions on the photon-energy scale associate the fragment firmly with the SCH processes dominant in these photon-energy regions. The resonance profiles show good agreements with previous works operating in the single-photon regime [5]. For iron-containing fragments involving bond breakage in the ligand, the broad resonance profiles suggest multiple relaxation pathways, which makes further claims on the fragments' origins difficult, and differs in ion yield from the work of Godehusen et al. O^{7+} is a special case among these fragments. Its resonance profile sharpens at high pulse energies and matches Figure 4 *b*. While this is mostly due to the natural absorption of O^{7+}, the increased ion yield towards 800 eV might be linked to the relaxation pathways involving DCH states.

References

[1] Martins, M. Photoionization of open-shell atoms: the chlorine 2p excitation. *Journal of Physics B: Atomic, Molecular and Optical Physics* **34**, 1321 (2001). URL https://dx.doi.org/10.1088/0953-4075/34/7/313.

[2] Martins, M. On the 3p→3d photoexcitation of atomic scandium. *Journal of Physics B: Atomic, Molecular and Optical Physics* **35**, L223 (2002). URL https://dx.doi.org/10.1088/0953-4075/35/11/101.

[3] Beerwerth, R. *et al.* Near L-edge Single and Multiple Photoionization of Triply Charged Iron Ions. *The Astrophysical Journal* **887**, 189 (2019). URL https://dx.doi.org/10.3847/1538-4357/ab5118. Publisher: The American Astronomical Society.

[4] Schippers, S. *et al.* Near L-edge Single and Multiple Photoionization of Doubly Charged Iron Ions. *The Astrophysical Journal* **908**, 52 (2021). URL https://dx.doi.org/10.3847/1538-4357/abcc64.

[5] Godehusen, K., Richter, T., Zimmermann, P. & Wernet, P. Iron L-Edge Absorption Spectroscopy of Iron Pentacarbonyl and Ferrocene in the Gas Phase. *The Journal of Physical Chemistry A* **121**, 66–72 (2017). URL https://doi.org/10.1021/acs.jpca.6b10399. Publisher: American Chemical Society.